PAPER

Check for updates

Sulfide glass solid-state electrolyte separators for Li metal batteries: using an interlayer to increase rate performance and reduce stack pressure†

Thomas A. Yersak, [ID] *[a] Chansoon Kang,[b] James R. Salvador,[a] Nicholas P. W. Pieczonka[a] and Mei Cai[a]

We report on the solubility of $(Li_2S)_{60}(SiS_2)_x(P_2S_5)_{40-x}$, $(0 \leq x \leq 40)$ sulfide glass solid-state electrolytes in the 1:1 (v/v) DME:DOL solvent mixture, a popular choice for lithium metal battery liquid electrolytes. SiS_2-rich glasses within the compositional range of $(Li_2S)_{60}(SiS_2)_x(P_2S_5)_{40-x}$ $(28 \leq x \leq 40)$ were found to be functionally insoluble in DME:DOL. Hybrid symmetric test cells with a thin liquid electrolyte layer (0.6 M LiTFSI + 0.4 M $LiNO_3$ in 1:1 (v/v) DME:DOL) at the interface between lithium metal electrodes and an insoluble $(Li_2S)_{60}(SiS_2)_{28}(P_2S_5)_{12}$ glass wafer were tested. Hybrid test cells delivered a critical current density of 3.0 mA cm^{-2} at 25 °C and 0.1 MPa, which is nearly double the CCD of comparable dry symmetric test cells cycled at 10× higher stack pressure.

1. Introduction

Solid-state electrolytes (SSE) are under investigation to enable Li metal anodes. Fully dense, defect free sulfide glasses have been shown to block Li metal dendrites.[1,2] However, one of the major challenges associated with solid-state batteries (SSBs) is the ability to obtain and maintain a low junction resistance at the SSE/Li interface. Recent work has shown that the mechanics of Li metal creep dictate that Li metal SSBs should be cycled under a stack pressure of > 1 MPa to achieve practical areal capacity and rates at room temperature.[3–5] In fact, Samsung's recently reported SSB utilized a 10 MPa stack pressure.[6] For comparison, conventional Li-ion pouch cells are cycled at <0.1 MPa stack pressure[7] and from the perspective of battery pack design it may be desired for SSBs to operate with similar specifications to those of conventional Li-ion batteries.

Fortunately, SSEs may be used in conjunction with other materials to alleviate the stack pressure requirement. For example, we previously integrated a $(Li_2S)_{60}(SiS_2)_{28}(P_2S_5)_{12}$ sulfide glass separator into a single layer Li–S pouch cell with a 1:1 (v/v) 1,2 dimethoxyethane (DME): 1,3 dioxolane (DOL) + 1 M LiTFSI liquid electrolyte (LE). The Li–P–Si–S glass was chosen for its low melt volatility and adequate stability *versus*

lithium.[1] The cell was cycled under a stack pressure of <0.05 MPa.[8] Similar hybrid cells, containing both LE and SSE, have also been reported with other SSEs such as $Li_{1.3}Al_{0.3}Ti_{1.7}(PO_4)_3$ (LATP), $Li_{1+x}Y_xZr_{2-x}(PO_4)_3$ (LYZP), $Li_{1.5}Al_{0.5}Ge_{1.5}(PO_4)_3$ (LAGP), and $Li_7La_3Zr_2O_{12}$ (LLZO).[9–12] Though the cells in these examples were flooded with LE, a small volume LE interlayer may sufficiently change the physics of Li stripping and plating to eliminate the >1 MPa stack pressure requirement.

At first glance, it is non-obvious that the $(Li_2S)_{60}$ $(SiS_2)_{28}(P_2S_5)_{12}$ sulfide glass would be stable in an ether-based LE. In fact, there have been at least two reports of sulfide SSEs precipitated from precursor solutions with ether-based solvents.[13,14] These SSE formulations, $(Li_2S)_{75}(P_2S_5)_{25}$ and $Li_{10}GeP_2S_{12}$, were also found to be soluble in triglyme.[15] Nonetheless, an ether-based LE was desired for two reasons. First, conventional Li-ion carbonate-based LEs are not compatible with the Li–S chemistry because sulfur may react with carbonates.[16] Second, $LiNO_3$ is an electrolyte additive that creates an effective SEI on Li metal that promotes efficient cycling.[17–19] Ether-based solvents are preferable because $LiNO_3$ has low solubility in carbonate solvents.[20]

In this study, we present a range of sulfide glass SSE compositions that are insoluble in ether based solvents. We then calculate glass weighted average bond dissociation enthalpies to predict each glass' relative solubility. We expect that our approach may inform the compatibility of a wide range of sulfide glass SSEs compositions with other solvents. Using this result we then show that a LE interlayer can concomitantly reduce the stack pressure requirement and increase critical current density (CCD).

[a] Chemical and Materials Systems Laboratory, General Motors Global R&D, 30500 Mound Rd., Warren, MI 48092-2031, USA. E-mail: thomas.yersak@gm.com; Tel: +01-586-320-8889

[b] Optimal, Inc., 47802 W. Anchor Ct., Plymouth, MI 48170, USA

2. Experimental

2.1 Glass synthesis, material characterization and solubility measurement

All precursors and products described in this work are hygroscopic so work was carried out in an argon-filled glovebox with a moisture level of <1 ppm. Glass precursors include P_2S_5 (Sigma-Aldrich, 99.9% powder), SiS_2 (American Elements, 99.0% powder), GeS_2 (American Elements, 99.0% powder), GeO_2 (American Elements, 99.0% powder) and Li_2S (Sigma-Aldrich, 99.8% powder). A range of glass compositions were prepared according to the equation, $(Li_2S)_{60}(SiS_2)_x(P_2S_5)_{40-x}$, where $x = 0, 4, 8, 12, 16, 20, 28, 40$. The glass with composition $(Li_2S)_{50}(GeS_2)_{45}(GeO_2)_5$ was also synthesized. To synthesize each glass electrolyte sample, 4 g of precursor powders were mixed in the appropriate stoichiometric ratios and pressed into 1 inch diameter pellets. Glasses were obtained by using one of two melt quenching methods chosen based on the volatility of each glass melt. In the first method the precursor pellet was loaded into a boron nitride (BN) crucible, capped with a quartz watch glass to minimize material loss by volatilization, and heated to 800–1000 °C for 30 minutes in a box furnace. Glass wafers of approximately 1 mm thickness were then formed by quenching the melt between a quartz glass and an agate anvil. The first method was used to synthesize glass compositions with low melt volatility; namely, $(Li_2S)_{60}(SiS_2)_x(P_2S_5)_{40-x}$ ($x = 28$, 40) and $(Li_2S)_{50}(GeS_2)_{45}(GeO_2)_5$. In the second method, precursor pellets were broken into pieces and loaded into carbon coated quartz ampoules (outer diameter = 8 mm). After flame sealing, the ampoules were heated to 800 °C for 30 minutes in a box furnace and quenched in oil. Using this method small ingots of approximately 5 mm diameter were obtained. The second method was used to synthesize glass compositions with high melt volatility; namely, $(Li_2S)_{60}(SiS_2)_x(P_2S_5)_{40-x}$ ($x = 0, 4$, 20), $(Li_2S)_{70}(P_2S_5)_{30}$ and $(Li_2S)_{75}(P_2S_5)_{25}$. SSEs with composition $(Li_2S)_{60}(SiS_2)_x(P_2S_5)_{40-x}$ ($x = 8, 12, 16$) were also synthesized by the second melt quenching method, but had poor glass formability. For this reason, these compositions are not included in this study. The $(Li_2S)_{60}(SiS_2)_x(P_2S_5)_{40-x}$ ($x = 28, 40$) compositions could not be synthesized by the second method because the melt was too corrosive to the quartz ampoule. The ionic conductivity of $(Li_2S)_{60}(SiS_2)_x(P_2S_5)_{40-x}$ glasses was previously reported.[34]

Samples were characterized to determine long range and short range order by X-ray diffraction (XRD, D8 Advance, Bruker, Cu-Kα (1.5406 Å) at room temperature) and Raman spectroscopy (Renishaw), respectively. X-Ray samples were prepared by sealing glass powder with Kapton film and Raman samples were prepared by loading glass powder in sealed quartz capillary tubes. The actual composition of splat quenched SiS_2-rich glasses was measured by energy dispersive spectroscopy (EDS, EDAX). We characterized the bulk composition of the glass by measuring 5 spots at the center of the glass' fracture surface.

The solubility of glass electrolyte samples was evaluated by immersing 150 mg of glass electrolyte in a 5 ml mixture of 1 : 1 (v/v) 1,2 dimethoxyethane (DME) (BASF) and 1,3 dioxolane (DOL) (BASF) and observing the change in color. Solvated species and the degree of solubility was quantified by Raman spectroscopy (Renishaw). Post processing of Raman spectra was carried out in the range of 330–520 cm^{-1}. The DOL : DME 1 : 1 (v/v) spectrum was used as a baseline for all spectra.

2.2 Solubility calculation

Whether a solute dissolves in a solvent at constant pressure and temperature is determined by eqn (1) where ΔG_{sol} is the Gibb's free energy of solution, ΔH_{sol} is the enthalpy of solution, T is temperature, and ΔS_{sol} is the entropy of solution. The enthalpy of solution and entropy of solution are described by eqn (2) and (3), respectively. The subscripts in each of these two equations refer to the three steps that take place in the formation of a solution; namely, (1) expanding the solute, (2) expanding the solvent, and (3) solvation.[33] The aim of this work was not treat the full free energy of solution, but rather to compare the relative solubility of glasses by deriving an expression that trends with the enthalpic term that varies the most with glass composition, namely, the enthalpy of solute expansion, ΔH_1.

This simplified treatment of solubility to explain experimental trends is reasonable since the other thermodynamic terms are expected to have a lesser impact as a function of glass composition. We acknowledge that there may be difference in the enthalpy of solvation between the SiS_x and PX_x and the ether based solvents. It is likely, based on Pauling electronegativities that Si–S bond would have a higher dipole moment compared to that of the P–S bond and we may therefore expect that SiS_x species to interact more strongly with polar groups of the ether solvents and be more exothermic in terms of solvation. Secondly, the bond lengths of Si–S and P–S are 192 and 212 pm, respectively, suggesting a larger and positive enthalpic contribution to solvent expansion for PS_x as compared to SiS_x units. With both of these considerations we might expect that SiS_2 rich species would be more soluble if the solute/solvent interactions and solute separation enthalpies dominated the resulting solubility behavior. However, since we will show that the more SiS_2 rich glasses are insoluble, we conclude that solute expansion and the interatomic interactions of the solute are principal contribution to the observed solubility behavior. We therefore expect the variation of ΔH_2 and ΔH_3 to be small compared to that of ΔH_1.

$$\Delta G_{sol} = \Delta H_{sol} - T\Delta S_{sol} \tag{1}$$

$$\Delta H_{sol} = \Delta H_1 - \Delta H_2 + \Delta H_3 \tag{2}$$

$$\Delta S_{sol} = \Delta S_1 + \Delta S_2 + \Delta S_3 \tag{3}$$

Two approaches were used for approximating the relative enthalpy of solute expansion, ΔH_1, by calculating the glass weighted average bond dissociation enthalpy (BDE_{wa}). The first approach is to simply use the mole fractions of the nominal glass composition and assume that each metalloid species (M) in the glass former constituent (M = P, Si or Ge) are all tetrahedrally coordinated by sulfur atoms thus forming 4 M–S

Table 1 List of common glass formers, their bonds of interest, its bond dissociation enthalpy and weighting value for the relevant number of bonds

Glass constituent	Bond	BDE (kJ mol^{-1})	Number of bonds (n)
P_2S_5	P–S	346	8
GeS_2	Ge–S	551	4
SiS_2	Si–S	619	4
GeO_2	Ge–O	658	4
Li_2S	Li–S	312	2

bonds while each Li_2S contributes 2 Li–S bonds. This simplification neglects contributions from Si, P and Ge homoatomic interactions. This approach is summarized in eqn (1) where m_i is the mole fraction of glass former, co-former and modifier. Furthermore, n_i is the number of bonds formed for each molecule of former, co-former and modifier. Literature values for the bond dissociation enthalpies (BDE) are taken from a variety of sources and listed in Table 1.[21–24] In the case of $(PS_4)^{-3}$ based moieties there are 3 single P–S bonds and 1 P–S double bond. The difference in BDE between P–S single and double bond is only 1 kJ mol^{-1} so are treated as equivalent. The denominator in eqn (1) reduces the expression to the weighted average of a single "composite bond" and allows the expression to be applied to any glass composition. This allows the comparison of bond strength over widely varying compositions within and across phase diagrams.

$$BDE_{wa} = \sum \frac{(m_i \times n_i \times BDE)}{\sum (m_i \times n_i)} \quad (4)$$

The second method of calculating the BDE_{wa} is to determine the mole fraction of each short-range order (SRO) structural moiety present in the glass, account for the number and type of bonds in each moiety and then use eqn (4) to calculate the BDE_{wa}. In this case, m_i is the mole fraction of the moiety and n_i is the number of M–S and M–M bonds within the moiety. This approach accounts for the homoatomic interactions but requires a great deal of structural detail of the glass in question. For this study we use a previously reported structural analysis for a similar glass compositional range $(Li_2S)_{60}(SiS_2)_x(P_2S_5)_{30-0.75x}$.[25,26]

### 2.3 Critical current density measurement

A Li/SSE/Li symmetric test cell was assembled to measure the critical current density (CCD) of a dense sulfide glass separator with liquid electrolyte interlayers at the Li electrolyte interfaces. The glass electrolyte composition of $(Li_2S)_{60}(SiS_2)_{28}(P_2S_5)_{12}$ was chosen based on the results of the solubility evaluation and unpolished glass wafer discs with about 1 mm thickness were prepared as described above. The liquid electrolyte was 1 : 1 (v/v) DME : DOL + 0.6 M bis(trifluoromethanesulfonyl)imide (LiTFSI) + 0.4 M lithium nitrate (LiNO₃). When soaked in this liquid electrolyte, a $(Li_2S)_{60}(SiS_2)_{28}(P_2S_5)_{12}$ glass wafer showed no evidence of dissolution after 2 years (Fig. S1, ESI†). The test cell housing consists of a modified $\frac{1}{2}''$ PTFE union fitting (Swagelok, PFA-820-6) and two $\frac{1}{2}''$ diameter PEEK rods with

13/64″ diameter stainless steel inserts. The stack pressure was measured using a force sensor as previously described.[27] The cell was assembled by stacking a glass electrolyte wafer between two 13/64″ diameter Li metal foil discs (Honjo, 100 μm thick on stainless steel). 6 μL of liquid electrolyte was applied to each electrode interface; enough to wet the interface, but not enough to flood the cell. 6. In dry cells, Li metal was applied to glass wafer surface by applying pressure to the stainless steel foil backing. In the hybrid cell, Li metal was simply stacked on top of the wetted glass wafer surface. The test cell was then cycled under progressively higher current densities (Arbin LBT-21084) until shorting failure was observed. Total cell resistance was calculated using Ohm's law. AC impedance could not be used to measure the relative values of bulk and interfacial impedance since equivalent circuits could not be fitted to the data due to significant hardware inductance at higher frequencies.

3. Results and discussion

3.1 Solubility

Prior to conducting the solubility experiment the long and short range structures of the samples with compositions $(Li_2S)_{60}(SiS_2)_x(P_2S_5)_{40-x}$ ($x = 0, 4, 20, 28, 40$) were characterized. All samples were determined to be amorphous according to pXRD measurement provided in Fig. 1. The short range structure for the glasses was characterized by Raman spectroscopy and the data are provided in Fig. 2. In agreement with the literature, the glasses were composed primarily of $Si_2S_5^{2-}$ (362 cm^{-1}), SiS_4^{4-} (385 cm^{-1}), $Si_2S_6^{4-}$ (408 cm^{-1}), $P_2S_6^{4-}$ (396 cm^{-1}), $P_2S_7^{4-}$ (404 cm^{-1}), and PS_4^{3-} (420 cm^{-1}) structural units.[25,26] For compositions $(Li_2S)_{60}(SiS_2)_x(P_2S_5)_{40-x}$ ($x = 0, 4, 20$) the actual composition is equivalent to the nominal composition because the precursors were melt quenched inside a sealed quartz ampoule. In this case, the samples lost zero mass during synthesis because melt vapors were confined within the ampoule. On the other hand, the $(Li_2S)_{60}(SiS_2)_x(P_2S_5)_{40-x}$ ($x = 28, 40$) samples experienced mass loss of 15.0% and 4.9%, respectively. A mass loss of 15% for the $(Li_2S)_{60}(SiS_2)_{28}(P_2S_5)_{12}$
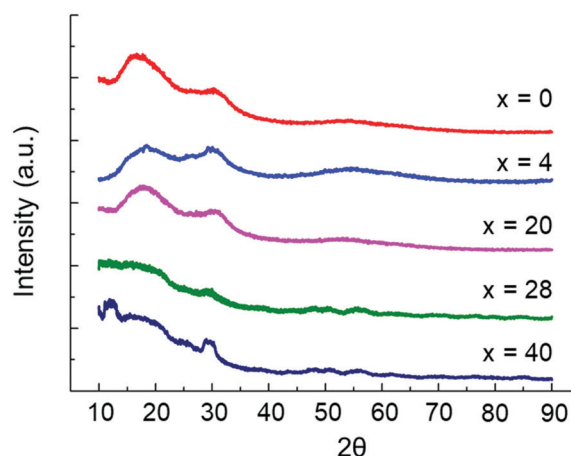
Fig. 1 pXRD of $(Li_2S)_{60}(SiS_2)_x(P_2S_5)_{40-x}$ ($x = 0, 4, 20, 28, 40$) samples indicate all compositions are amorphous.
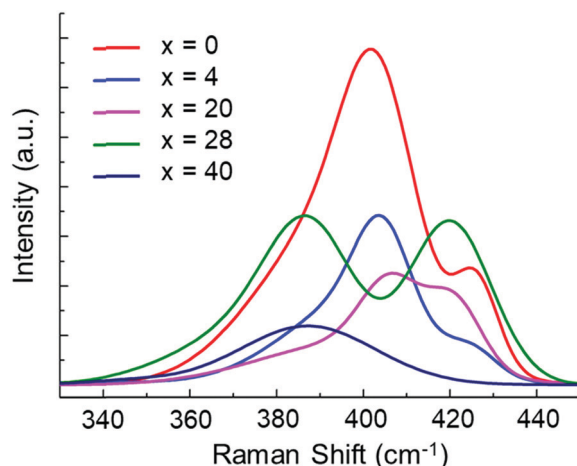
Fig. 2 Raman spectra of glass compositions $(Li_2S)_{60}(SiS_2)_x(P_2S_5)_{40-x}$ (x = 0, 4, 20, 28, 40).

composition is similar to that reported by a previous study.[1] The actual compositions for $(Li_2S)_{60}(SiS_2)_x(P_2S_5)_{40-x}$ (x = 28, 40) as determined by EDS are provided in Table 2 and only deviate slightly from the actual composition.

The results of the solubility experiment are provided in Fig. 3. After only 1 hour, the P_2S_5-rich glasses, $(Li_2S)_{60}(SiS_2)_x(P_2S_5)_{40-x}$ (x = 0, 4), partially dissolved as evidenced by the DME : DOL solvent's yellow color. After two weeks, the $(Li_2S)_{60}(SiS_2)_{20}(P_2S_5)_{20}$ composition also showed evidence of dissolution. On the other hand, the DME : DOL solvent for the SiS_2-rich glasses, $(Li_2S)_{60}(SiS_2)_x(P_2S_5)_{40-x}$ (x = 28, 40), remained clear for the entire testing period. After two weeks, the remaining solids were collected from each solution and weighed (Fig. 4). The color of the $(Li_2S)_{60}(P_2S_5)_{40}$ sample changed from dark yellow to light yellow and the $(Li_2S)_{60}(SiS_2)_x(P_2S_5)_{40-x}$ (x = 4, 20) samples turned white. On the other hand, the $(Li_2S)_{60}(SiS_2)_x(P_2S_5)_{40-x}$ (x = 28, 40) samples were completely intact. While the x = 0, 4, and 20 samples experienced mass loss of 95%, 32%, and 16%, respectively, the x = 28, 40 samples had zero mass loss. It was concluded that P_2S_5-rich compositions were susceptible to dissolution in a DME : DOL co-solvent. In addition, the solubilities of two other SSEs were tested in DME : DOL. A glass ingot of $(Li_2S)_{50}(GeS_2)_{45}(GeO_2)_5$, prepared as previously described,[28] was insoluble while $Li_{10}GeP_2S_{12}$ (NEI Corporation) was slightly soluble.

The solubility of each glass composition was further quantified with Raman spectroscopy and the data are provided in Fig. 5. Fig. 5a provides the Raman spectra of all samples and neat 1 : 1 (v/v) DME : DOL in the range of 100–500 cm^{-1}. The
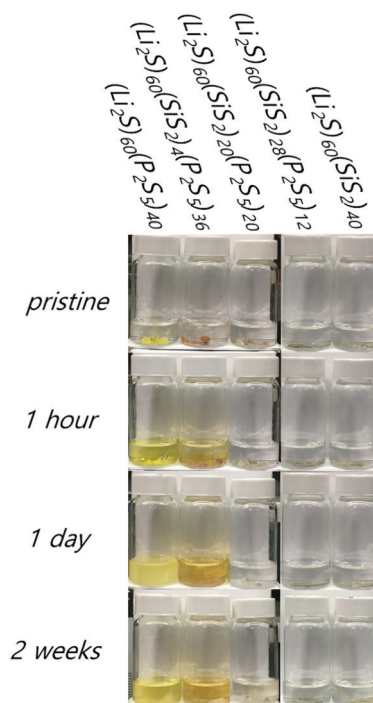
Table 2 Quantified nominal and actual composition for SiS_2-rich splat quenched glasses

Sample, $(Li_2S)_{60}(SiS_2)_x(P_2S_5)_{40-x}$	Method	P (%)	S (%)	Si (%)
x = 28	Calc.	10.5	77.2	12.3
	EDS	9.0	74.3	16.7
x = 40	Calc.	—	77.8	22.2
	EDS	—	75.4	24.6

Fig. 3 Solubility times series for $(Li_2S)_{60}(SiS_2)_x(P_2S_5)_{40-x}$ (x = 0, 4, 20, 28, 40) glasses soaked in 1 : 1 (v/v) DME : DOL. After 2 weeks the x = 0, 4 and 20 sample solutions show signs of discoloration, which is attributed to dissolution of the glass. The x = 28 and 40 sample solutions remain clear over the course of the experiment.
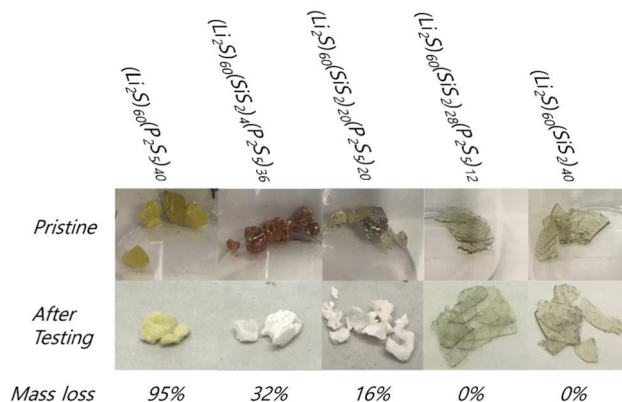

Fig. 4 Pictures of $(Li_2S)_{60}(SiS_2)_x(P_2S_5)_{40-x}$ (x = 0, 4, 20, 28, 40) samples before and after solubility testing in 1 : 1 (v/v) DME : DOL for 2 weeks. The x = 0, 4 and 20 samples experienced mass loss of 95%, 32% and 16%, respectively, whereas the x = 28 and 40 samples experienced no mass change.

spectra are normalized to a strong C–O vibrational mode from DOL : DME mixture at 940 cm^{-1} (not shown).[29,30] Generally, the vibrational modes below 200 cm^{-1} and around 450 cm^{-1} are attributable to sulfur species,[31] while the vibrational modes in the 350–450 cm^{-1} range are attributable to solvated glass structural units $(P_2S_6)^{4-}$, $(P_2S_7)^{4-}$, and $(PS_4)^{3-}$.[25,26] A vibrational mode of DME, centered at 365 cm^{-1}, is minorly convolved with

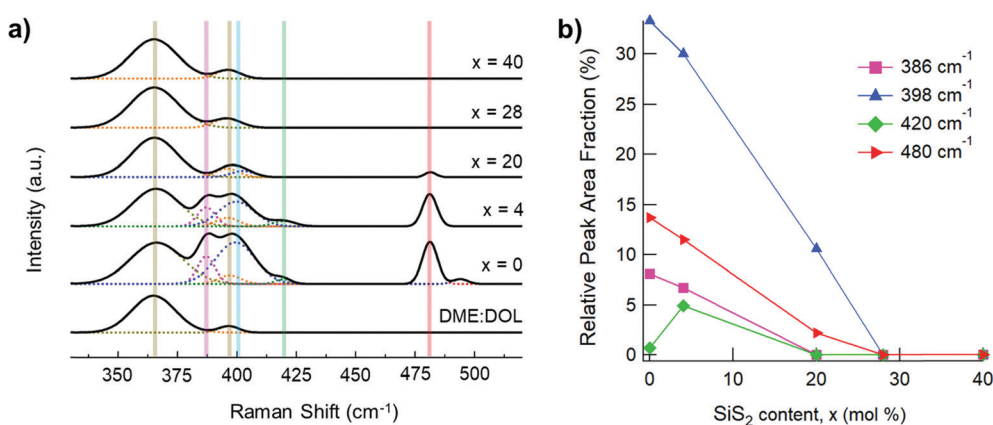Fig. 5 (a) Raman spectra of pristine DOL : DME solvent and solutions obtained by soaking $(Li_2S)_{60}(SiS_2)_x(P_2S_5)_{40-x}$ (x = 0, 4, 20, 28, 40) glasses in DME : DOL. The location of structural unit vibrational modes are indicated with colored bars from left to right; namely, $P_2S_7^{4-}$ (pink), $P_2S_6^{4-}$ (blue), PS_4^{3-} (green), and S_8 (orange). Two vibrational modes of DME : DOL are also indicated (brown). (b) Summary of dissolved species as a function of glass composition.

the structural units' vibrational modes, but does not impact analyses. Since several unidentified vibrational modes are observed in the 220–330 cm^{-1} range, our analysis therefore focuses on the range of 330–520 cm^{-1}. The peaks at 387, 398, 420 and 480 cm^{-1} are attributed to vibrational modes of $(P_2S_6)^{4-}$, $(P_2S_7)^{4-}$, $(PS_4)^{3-}$, and S_8, respectively.[25,26,31] P_2S_5-rich glasses, $(Li_2S)_{60}(SiS_2)_x(P_2S_5)_{40-x}$ (x = 0, 4), showed the highest prevalence of $(P_2S_6)^{4-}$, $(P_2S_7)^{4-}$, $(PS_4)^{3-}$, and S_8 species. On the other hand, the spectra for the SiS$_2$-rich glasses, $(Li_2S)_{60}(SiS_2)_x(P_2S_5)_{40-x}$ (x = 28, 40), were indistinguishable from the spectrum for neat 1 : 1 (v/v) DME : DOL suggesting the complete absence of solvated SSE species. With the exception of PS_4^{3-}, solvated SSE species decrease linearly with increasing SiS$_2$, x (Fig. 5b). The non-linear prevalence of PS_4^{3-} with respect to x can be explained by the structural composition of the pristine glass samples (Fig. 2) wherein PS_4^{3-} is not present in the $(Li_2S)_{60}(P_2S_5)_{40}$ (x = 0) composition. With this result we show that the $(Li_2S)_{60}$ $(SiS_2)_{28}(P_2S_5)_{12}$ glass is functional insoluble in DME : DOL. It is

possible that this glass composition exhibits a small degree of solubility, however, it was below the detection limit or our equipment.

3.2 BDE$_{WA}$ calculation

As discussed in the Methods section, solubility is governed in part by the enthalpy of solute expansion, ΔH_1, which is a measure of the solute's interatomic bond strength. To that end, we conjecture that the relative insolubility of glasses can be estimated by calculating a weighted average bond dissociate energy, BDE$_{wa}$, for each glass composition. As outlined in the Methods section we take two approaches to compute the BDE$_{wa}$. The first approach calculates an approximate BDE$_{wa}$ using only the nominal glass composition, while the second approach is more exact since it uses the glass SRO structural moiety composition. To calculate BDE$_{wa}$ with the second approach, we use a SRO dataset for Li$_2$S–SiS$_2$–P$_2$S$_5$ glasses

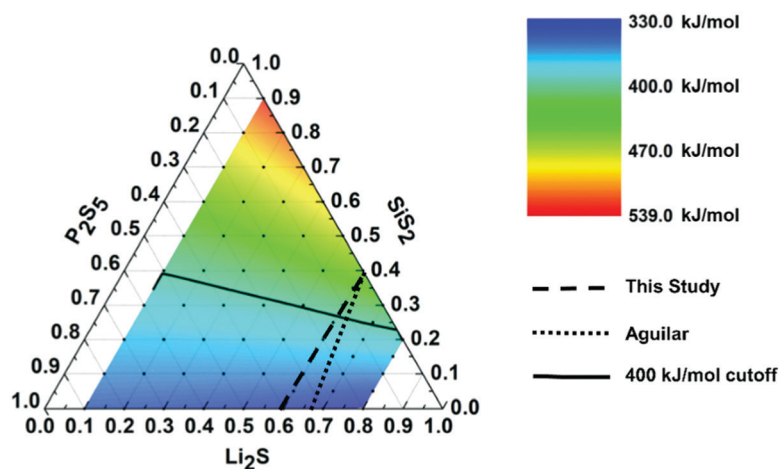Fig. 6 Ternary phase diagram with BDE$_{wa}$ mapping. The solid line represents the 400 kJ mol^{-1} cutoff line, below which, the compositions are predicted to be soluble in DME : DOL. The dashed line depicts the $(Li_2S)_{60}(SiS_2)_x(P_2S_5)_{40-x}$ compositions used in this study while the dotted line depicts the previously reported $(Li_2S)_{60}(SiS_2)_x(P_2S_5)_{30-0.75x}$ compositions.[25,26]

previously reported by Aguilar.[26] The glass compositions explored by Aguilar differ slightly from this study as shown in the ternary phase diagram presented in Fig. 6. Nonetheless, we chose to use the Aguilar's SRO dataset because it was compiled using both Raman, IR, and NMR Spectroscopy, whereas this study's SRO dataset is incomplete since it was compiled with only Raman Spectroscopy. Using this previously reported SRO dataset, we will first show that there is not a significant difference between the two BDE_{wa} calculation methods.

Aguilar[26] identifies seven SRO moieties present in glass compositions described by the formula, $(Li_2S)_{60}(SiS_2)_x$ $(P_2S_5)_{30-0.75x}$, $(0 \leq x \leq 40)$. Table 3 summarizes the approximate relative abundance (%) for each of these seven SRO units for compositions in the range $(Li_2S)_{60}(SiS_2)_x(P_2S_5)_{30-0.75x}$.[26] The BDE_{wa} for each glass composition was calculated using the values in Table 3 and eqn (4). For the calculations we assume that each Li_2S contributes 2 Li–S bonds and so the mole fraction of the modifier is multiplied by 2 and by the BDE of the Li–S bond. The calculated SRO BDE_{wa}'s are provided in the second column of Table 4. As expected, the SRO BDE_{wa} increases with increasing SiS_2 content since the Si–S bond is comparatively stronger than the P–S bond.

Despite the diversity of the SRO units that comprise chalcogenide glasses, the number of M–S bonds (M = P, Si, Ge) is fixed at 4 per metalloid/chalcogenide center with the exception of P_2S_6 and Si_2S_6 SRO units. We can therefore compute the BDE_{wa} by using the nominal glass composition of modifier, former, and co-formers. This approach ignores the P–P bonds in P_2S_6 and the Si–Si bonds in Si_2S_6 since the contribution of these bonds to the BDE_{wa} is small. Specifically, the relative abundances of the P_2S_6 and Si_2S_6 units in most glasses is low and the M–M bond is only 1 part in 7 bonds within each unit. The nominal BDE_{wa}'s for all glass compositions are provided in the third column of Table 4. There is good agreement between the SRO BDE_{wa} and nominal BDE_{wa}.

Having established that the nominal glass composition is adequate for the calculation of BDE_{wa} using Aguilar's similar glass system, we then computed the BDE_{wa} for our glass system, $(Li_2S)_{60}(SiS_2)_x(P_2S_5)_{40-x}$. The BDE_{wa} for this study's glass compositions are listed in the third column of Table 4. The same trend emerges in that the BDE_{wa} increases as the SiS_2 content increases. The results listed in Table 4 combined with those of the solubility study would seem to indicate that a BDE_{wa} threshold value of > 400 kJ mol^{-1} is associated with glass compositions that are insoluble in DME:DOL. Using the nominal composition allows for the calculation of BDE_{wa} for an entire phase diagram so that one can locate a compositional

Table 4 Results of BDE_{wa} calculations for previously reported glass compositions[26] and for this study's glass composition. Also listed are the the values computed for a Li–Ge–S–O glass and the LGPS ceramic SSE

Nominal glass composition (mol%)	BDE_{wa} (kJ mol^{-1}) SRO composition	BDE_{wa} (kJ mol^{-1}) Nominal composition
$(Li_2S)_{60}(SiS_2)_{40}$	487	489
$(Li_2S)_{61.86}(SiS_2)_{28.87}(P_2S_5)_{9.28}$	433	431
$(Li_2S)_{63.16}(SiS_2)_{21.05}(P_2S_5)_{15.79}$	408	412
$(Li_2S)_{65.93}(SiS_2)_{4.40}(P_2S_5)_{29.67}$	347	348
$(Li_2S)_{67}(P_2S_5)_{33}$	336	335
$(Li_2S)_{60}(SiS_2)_{28}(P_2S_5)_{12}$	N/A	427
$(Li_2S)_{60}(SiS_2)_{20}(P_2S_5)_{20}$	N/A	395
$(Li_2S)_{60}(SiS_2)_{4}(P_2S_5)_{36}$	N/A	347
$(Li_2S)_{60}(P_2S_5)_{40}$	N/A	339
$(Li_2S)_{50}(GeS_2)_{45}(GeO_2)_5$	479	479
$Li_{10}GeP_2S_{12}$	375	N/A

space in which formulations are likely to be insoluble in DME:DOL without laboriously identifying and quantifying all SRO units for each composition. Fig. 6 presents a contour ternary phase diagram for $Li_2S·SiS_2·P_2S_5$ glasses. The color mapping visualizes the BDE_{wa} for each ternary composition allowing us to visualize the compositional regions where the BDE_{wa} is > 400 kJ mol^{-1} and therefore anticipated to be compatible with DME:DOL solvents.

Next, we extend our approach to GeS_2-based glasses[28] and the LGPS ($Li_{10}GeP_2S_{12}$) ceramic superionic SSE.[32] We find that the BDE_{wa} for $(Li_2S)_{50}(GeS_2)_{45}(GeO_2)_5$, a formulation we know to be insoluble in DME:DOL (Fig. S2, ESI†), has a very high BDE_{wa} of 479 kJ mol^{-1}. This is based on the fact that $(Li_2S)_{50}(GeS_2)_{45}$ $(GeO_2)_5$ is composed exclusively of $(GeS_4)^{2-}$ SROs with O atoms mixed on the sulfur sites.[28] This result is consistent with our insolubility selection criteria of $BDE_{wa} > 400$ kJ mol^{-1}. The LGPS ceramic, which is known to be composed of a network of one $(GeS_4)^{4-}$ and two $(PS_4)^{3-}$ tetrahedral units, has a BDE_{wa} of 375 kJ mol^{-1}. We note that the BDE_{wa} calculated for LGPS and $(Li_2S)_{60}(SiS_2)_{20}(P_sS_5)_{20}$ are within 20 kJ mol^{-1} of each other and that both SSEs are weakly soluble in DME-DOL solutions.

Recent work by Oh et al. examined the dual solid–liquid electrolyte systems of $(Li_2S)_{75}(P_2S_5)_{25}$ (LPS) or LGPS in combination with a highly concentrated solution of LiTFSI in triglyme, which is an ether based solvent.[15] Here, it was found that both LPS and LGPS were soluble in neat triglyme but that the solubility could be decreased by increasing the concentration of LiTFSI. Oh et al. argue that the Li$^+$ of the TFSI$^-$ coordinated with the O atoms in the glyme and therefore reduced the propensity for nucleophilic attack on the P-atoms in the SSE. Lower LiTFSI concentrations were required to

Table 3 List of the glass compositions and the relative abundance (%) of each SRO moiety as previously reported.[26]

Composition/SRO	$(SiS_4)^{4-}$	$(Si_2S_4)^{2-}$	$(SiS_4)^{2-}$	$(Si_2S_6)^{-6}$	$(P_2S_7)^{4-}$	$(P_2S_6)^{4-}$	$(PS_4)^{3-}$
$(Li_2S)_{60}(SiS_2)_{40}$	59	12	17	12	0	0	0
$(Li_2S)_{61.86}(SiS_2)_{28.87}(P_2S_5)_{9.28}$	25	20	15	5	5	5	25
$(Li_2S)_{63.16}(SiS_2)_{21.05}(P_2S_5)_{15.79}$	10	20	10	5	5	10	40
$(Li_2S)_{65.93}(SiS_2)_{4.40}(P_2S_5)_{29.67}$	0	5	3	2	70	15	5
$(Li_2S)_{67}(P_2S_5)_{33}$	0	0	0	0	85	15	0

stabilize the LGPS in the glyme and the authors argued that hard-soft acid base theory favored stronger nucleophilic attack on the P sites in LPS glass by O as compared to the Ge sites in LGPS glass. We argue here that the differences in solubility observed in their work may also be explained by the average strength of the bonds in the solute. By our method, LPS has a BDE_{wa} of 331 kJ mol^{-1}, which is $\sim$13% lower than LGPS' BDE_{wa} of 375 kJ mol^{-1}. Consistent with Oh *et al.*'s observations, our method predicts that both SSEs are soluble in ethers, but that LGPS will have a lower solubility since it has the higher BDE_{wa}.

In our compositions, the nucleophilic centers (Si and P) are both hard acids and therefore should be more amenable to attack by O in the ether solvents. Instead, we find that certain SiS_2 rich glasses are functionally insoluble in DME : DOL. Based on these observations we argue that the difference in solubility behavior is due to the average bond strength of the solute and not just its hard or soft acidic nature. Further supporting this argument is the observation that glass formulations with BDE_{wa} less than, but close to, 400 kJ mol^{-1} dissolve far more slowly than those with BDE_{wa} well below 400 kJ mol^{-1}. We believe that this approach is generally applicable to other glass former systems and that it can be used as a criterion for selecting glass and ceramic compositions that are insoluble in ether based solvent systems often used in Li–S battery chemistries.

3.3 Critical current density measurement

Having established the functional insolubility of a range of sulfide glass, we then sought to demonstrate a practical use for our findings. For this work, the $(Li_2S)_{60}(SiS_2)_{28}(P_2S_5)_{12}$ glass composition was carried forward due to its functional insolubility, its high ionic conductivity of 1.8 mS cm^{-1}, and the availability of a baseline dataset.[1,8] As previously discussed, recent work establishes the need for a high stack pressure ($>$1 MPa) to maintain the integrity of the SSE/Li metal interface.[1,3–5] When cycled under a stack pressure of 0.1 MPa at 25 °C, the voltage response of a dry symmetric Li/SSE/Li test cell increased rapidly at an applied current density of 600 µA cm^{-2} (Fig. 7a).[1] The rapidly increasing voltage response may be explained by contact failure. Mechanical creep is the predominant mechanism for the mass transport of Li metal to the SSE interface and contact failure occurs when the rate of Li stripping outpaces the rate of interfacial Li replenishment by mechanical creep.[3,4] As a result, voids form at the SSE interface causing the eventual detachment of the electrode and an increase in cell resistance. The rate of creep is influenced both by temperature and applied pressure. When the stack pressure is increased to 3.0 MPa, but the temperature kept at 25 °C, the CCD of a similar Li/SSE/Li test cells increases to $\geq$ 1400 µA cm^{-2} (Fig. 7b) with failure attributed to shorting.[1] While higher stack pressures allow for practical current densities, battery packs with conventional Li-ion pouch cells apply stack pressures of $<$0.1 MPa.[7] From the perspective of pack design, it may therefore be desired for advanced batteries with SSE to operate under similarly low stack pressure specifications.

In this study, a small amount of 1 : 1 (v/v) DME : DOL + 0.6 M LiTFSI + 0.4 M LiNO$_3$ liquid electrolyte (LE) was applied to the
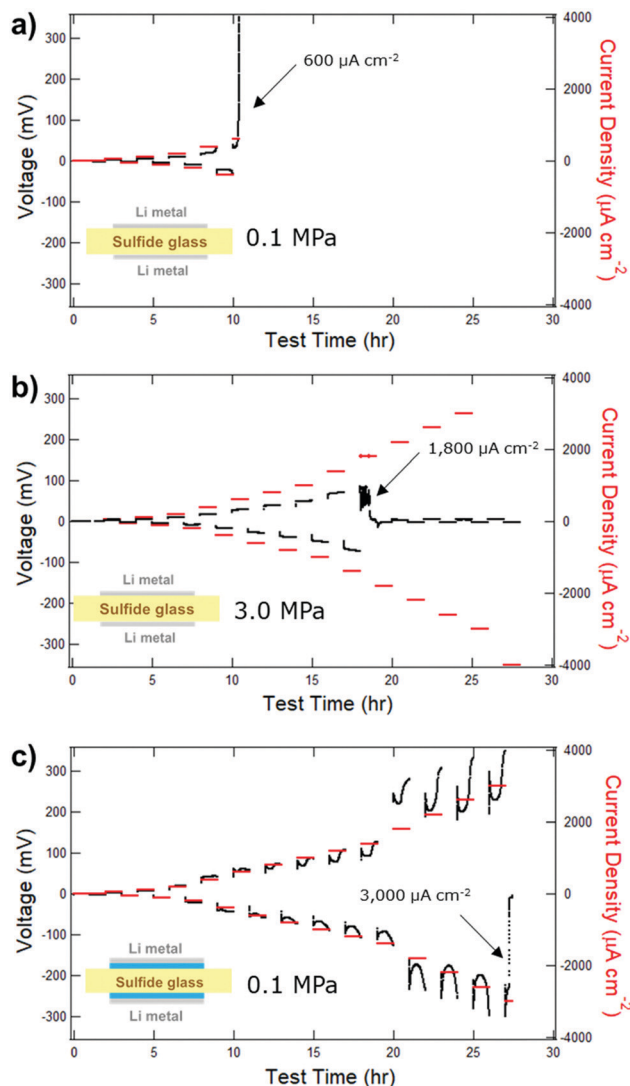

Fig. 7 CCDs of symmetric Li/SSE/Li test cells with or without a liquid electrolyte interlayer and a different stack pressures at 25 °C. The SSE separators are $(Li_2S)_{60}(SiS_2)_{28}(P_2S_5)_{12}$ glass wafers of approximately 600 µm thickness. (a) A test cell with direct Li/SSE contact and 0.1 MPa stack pressure experiences electrode contact failure at a CCD of 600 µA cm^{-2}.[1] (b) A test cell with direct Li/SSE contact and 3 MPa stack pressure experiences shorting failure at a CCD of 1800 µA cm^{-2}.[1] (c) A hybrid test cell with liquid electrolyte Li/SSE interlayer and a 0.1 MPa stack pressure experiences shorting failure at a CCD of 3000 µA cm^{-2}. Note: the test was paused for two days at 20 hours due to a planned facility power outage.

Li/SSE interfaces (blue layer, Fig. 7c – inset). A hybrid symmetric Li/LE/SSE/LE/Li test cell cycled with a stack pressure of only 0.1 MPa at 25 °C had a CCD of 3000 µA cm^{-2}. A second test cell (Fig. S3, ESI†) had a CCD of 2600 µA cm^{-2}, thus confirming the repeatability of our experiment. With these data, it is understood that a liquid electrolyte interlayer concomitantly decreases the stack pressure requirement and increases the CCD. Pictures of a glass wafer separator *post-mortem* (Fig. S4, ESI†) show that the wafer surface is the same color and transparency as a pristine, uncycled wafer. A short is evident

along a fracture surface of the wafer suggesting that sulfide glass separator fracture toughness should be improved.

Conclusions

In this work we demonstrated that sulfide glass SSE separators can be paired with an ether-based liquid electrolyte interlayer to increase critical current density while concomitantly decreasing stack pressure. Future work involves understanding the cycle life and safety of similarly designed hybrid test cells and investigating other liquid electrolyte formulations. Furthermore, we presented the BDE_{wa} calculation as a method to predict the compatibility of sulfide SSEs with organic solvents. As the solid-state battery community shifts its focus from the laboratory to the development of large scale manufacturing processes, our method may also hold value for predicting how sulfide SSEs interact with solvents used for carrying slurries or dissolving binders.

Conflicts of interest

The authors have no external funding sources or competing interests to declare.

Acknowledgements

References

1 T. A. Yersak, J. R. Salvador, N. P. W. Pieczonka and M. Cai, Dense, Melt Cast Sulfide Glass Electrolyte Separators for Li Metal Batteries, *J. Electrochem. Soc.*, 2019, **166**(8), A1535–A1542.

2 L. Porz, T. Swamy, B. W. Sheldon, D. Rettenwander, T. Frömling, H. L. Thaman, S. Berendts, R. Uecker, W. C. Carter and Y.-M. Chiang, Mechanism of lithium metal penetration through inorganic solid electrolytes, *Adv. Energy Mater.*, 2017, **20**, 1701003.

3 W. S. LePage, Y. Chen, E. Kazyak, K.-H. Chen, A. J. Sanchez, A. Poli, E. M. Arruda, M. D. Thouless and N. P. Dasgupta, Lithium Mechanics: Roles of Strain Rate and Temperature and Implications for Lithium Metal Batteries, *J. Electrochem. Soc.*, 2019, **166**(2), A89.

4 A. Masias, N. Felten, R. Garcia-Mendez, J. Wolfenstine and J. Sakamoto, Elastic, Plastic, and Creep Mechanical Properties of Lithium Metal, *J. Mater. Sci.*, 2019, **54**(3), 2585–2600.

5 J. Kasemchainan, S. Zekoll, D. Spencer Jolly, Z. Ning, G. O. Hartley, J. Marrow and P. G. Bruce, Critical Stripping Current Leads to Dendrite Formation on Plating in Lithium Anode Solid Electrolyte Cells, *Nat. Mater.*, 2019, **18**(10), 1105–1111.

6 Y.-G. Lee, S. Fujiki, C. Jung, N. Suzuki, N. Yashiro, R. Omoda, D.-S. Ko, T. Shiratsuchi, T. Sugimoto and S. Ryu, High-Energy Long-Cycling All-Solid-State Lithium Metal Batteries Enabled by Silver–Carbon Composite Anodes, *Nat. Energy*, 2020, **5**(4), 299–308.

7 Y. C. Zhang; O. Briat; J.-Y. Deletage; C. Martin; G. Gager and J.-M. Vinassa Characterization of External Pressure Effects on Lithium-Ion Pouch Cell. In *2018 IEEE International Conference on Industrial Technology (ICIT)*; IEEE, 2018; pp. 2055–2059.

8 T. Yersak, J. R. Salvador, R. D. Schmidt and M. Cai, Hybrid Li-S Pouch Cell with a Reinforced Sulfide Glass Solid-State Electrolyte Film Separator, *Int. J. Appl. Glas. Sci.*, 2021, **12**(1), 124–134.

9 L. Wang, Y. Wang and Y. Xia, A High Performance Lithium-Ion Sulfur Battery Based on a Li_2S Cathode Using a Dual-Phase Electrolyte, *Energy Environ. Sci.*, 2015, **8**(5), 1551–1558.

10 X. Yu, Z. Bi, F. Zhao and A. Manthiram, Hybrid Lithium − Sulfur Batteries with a Solid Electrolyte Membrane and Lithium Polysulfide Catholyte, *ACS Appl. Mater. Interfaces*, 2015, **7**, 16625–16631.

11 Q. Wang, Z. Wen, J. Jin, J. Guo, X. Huang, J. Yang and C. Chen, A Gel-Ceramic Multi-Layer Electrolyte for Long-Life Lithium Sulfur Batteries, *Chem. Commun.*, 2016, **52**(8), 1637–1640.

12 X. Yu, Z. Bi, F. Zhao and A. Manthiram, Polysulfide-Shuttle Control in Lithium-Sulfur Batteries with a Chemically/Electrochemically Compatible NaSICON-Type Solid Electrolyte, *Adv. Energy Mater.*, 2016, 1601392.

13 H. Lim, H. Lim, X. Xing, B. Lee, H. Liu, C. Coaty, H. Kim and P. Liu, Solid Electrolyte Layers by Solution Deposition, *Adv. Mater. Interfaces*, 2018, **5**(8), 1701328.

14 Q. Xiao, M. Cai, J. R. Salvador, L. Yang and D. A. I. Fang Electrolyte and Electrode Structure. Google Patents June 16, 2016.

15 D. Y. Oh, Y. J. Nam, K. H. Park, S. H. Jung, S. Cho, Y. K. Kim, Y. Lee, S. Lee and Y. S. Jung, Excellent Compatibility of Solvate Ionic Liquids with Sulfide Solid Electrolytes: Toward Favorable Ionic Contacts in Bulk-Type All-Solid-State Lithium-Ion Batteries, *Adv. Energy Mater.*, 2015, **5**(22), 1500865.

16 J. Gao, M. A. Lowe, Y. Kiya and H. D. Abruna, Effects of Liquid Electrolytes on the Charge–Discharge Performance of Rechargeable Lithium/Sulfur Batteries: Electrochemical and in-Situ X-Ray Absorption Spectroscopic Studies, *J. Phys. Chem. C*, 2011, **115**(50), 25132–25137.

17 Y. V. Mikhaylik Electrolytes for Lithium Sulfur Cells. Google Patents April 8, 2008.

18 S. S. Zhang, Role of $LiNO_3$ in Rechargeable Lithium/Sulfur Battery, *Electrochim. Acta*, 2012, **70**, 344–348.

19 B. D. Adams, E. V. Carino, J. G. Connell, K. S. Han, R. Cao, J. Chen, J. Zheng, Q. Li, K. T. Mueller and W. A. Henderson, Long Term Stability of Li-S Batteries Using High Concentration Lithium Nitrate Electrolytes, *Nano Energy*, 2017, **40**, 607–617.

20 Z. L. Brown, S. Heiskanen and B. L. Lucht, Using Triethyl Phosphate to Increase the Solubility of $LiNO_3$ in Carbonate Electrolytes for Improving the Performance of the Lithium Metal Anode, *J. Electrochem. Soc.*, 2019, **166**(12), A2523.

21 T. L. Cottrell, *The Strengths of Chemical Bonds*, Butterworth, London, 2nd edn, 1958.

22 B. Darwent deB. *Bond Dissociation Energies in Simple Molecules*, National Standard Reference Data Series; Washington, 1970.

23 S. W. Benson, III-Bond Energies, *J. Chem. Educ.*, 1965, **42**(9), 502.

24 J. A. Kerr, Bond Dissociation Energies by Kinetic Methods, *Chem. Rev.*, 1966, **66**(5), 465–500.

25 R. Zhao, S. Kmiec, G. Hu and S. W. Martin, Lithium Thiosilicophosphate Glassy Solid Electrolytes Synthesized by High-Energy Ball-Milling and Melt-Quenching: Improved Suppression of Lithium Dendrite Growth by Si Doping, *ACS Appl. Mater. Interfaces*, 2019, **12**(2), 2327–2337.

26 M. A. P. Aguilar, *Characterization of Lithium Thiosilicophosphate Glasses Prepared by High Energy Ball Milling*, Dissertation, Iowa State University, 2018.

27 T. Yersak, J. R. Salvador, R. D. Schmidt and M. Cai, Hot Pressed, Fiber-Reinforced $(Li_2S)_{70}(P_2S_5)_{30}$ Solid-State Electrolyte Separators for Li Metal Batteries, *ACS Appl. Energy Mater.*, 2019, **2**(5), 3523–3531.

28 Y. Kim, J. Saienga and S. W. Martin, Anomalous Ionic Conductivity Increase in $Li_2S + GeS_2 + GeO_2$ Glasses, *J. Phys. Chem. B*, 2006, **110**(33), 16318–16325.

29 V. Mohaček-Grošev, K. Furić and H. Ivanković, Observed Bands in Raman and Infrared Spectra of 1,3-Dioxolane and Their Assignments, *Vib. Spectrosc.*, 2013, **64**, 101–107.

30 P. J. Victor, B. Das and D. K. Hazra, A Study on the Solvation Phenomena of Some Sodium Salts in 1,2-Dimethoxyethane from Conductance, Viscosity, Ultrasonic Velocity, and FT-Raman Spectral Measurements, *J. Phys. Chem. A*, 2001, **105**(24), 5960–5964.

31 W. Zhu, A. Paolella, C. S. Kim, D. Liu, Z. Feng, C. Gagnon, J. Trottier, A. Vijh, A. Guerfi, A. Mauger, C. M. Julien, M. Armand and K. Zaghib, Investigation of the Reaction Mechanism of Lithium Sulfur Batteries in Different Electrolyte Systems by: *In Situ* Raman Spectroscopy and in Situ X-Ray Diffraction, *Sustainable Energy Fuels*, 2017, **1**(4), 737–747.

32 N. Kamaya, K. Homma, Y. Yamakawa, M. Hirayama, R. Kanno, M. Yonemura, T. Kamiyama, Y. Kato, S. Hama and K. Kawamoto, A Lithium Superionic Conductor, *Nat. Mater.*, 2011, **10**(9), 682–686.

33 S. S. Zumdahl, *Chemical Principles*, Houghton Mifflin Co., Boston, 5th edn, 2005.

34 J. H. Kennedy and Z. Zhang, Preparation and Electrochemical Properties of the $SiS_2–P_2S_5–Li_2S$ Glass Coformer System, *J. Electrochem. Soc.*, 1989, **136**(9), 2441.